PHOTONICS Research

Influence of mixed organic cations on the nonlinear optical properties of lead tri-iodide perovskites

Xuanyu Zhang,[1] Shuyu Xiao,[2] Ruxue Li,[1] Tingchao He,[2,5] Guichuan Xing,[3,6] and Rui Chen[1,4,7]

[1]Department of Electrical and Electronic Engineering, Southern University of Science and Technology, Shenzhen 518055, China
[2]College of Physics and Optoelectronic Engineering, Shenzhen University, Shenzhen 518060, China
[3]Joint Key Laboratory of the Ministry of Education, Institute of Applied Physics and Materials Engineering, University of Macau, Avenida da Universidade, Taipa, Macau 999078, China
[4]Key Laboratory of Energy Conversion and Storage Technologies (Southern University of Science and Technology), Ministry of Education, Shenzhen 518055, China
[5]e-mail: tche@szu.edu.cn
[6]e-mail: gcxing@um.edu.mo
[7]e-mail: chenr@sustech.edu.cn

Received 1 June 2020; revised 1 July 2020; accepted 1 July 2020; posted 7 July 2020 (Doc. ID 398975); published 17 August 2020

Metal halide perovskite materials have been widely studied recently due to their excellent optoelectronic properties. Among these materials, organic-inorganic hybrid perovskites have attracted much attention because of their relatively soft framework, which makes them more suitable for nonlinear optical (NLO) applications. However, there is rare physical mechanism study on the coexistence of two-photon absorption (TPA) and saturable absorption (SA) in organic-inorganic hybrid perovskite materials. To clarify this issue, the NLO properties of mixed cation perovskite $MA_{1-x}FA_xPbI_3$ [MA = CH_3NH_3, FA = $CH(NH_2)_2$, x = 0, 0.2, 0.4, 0.6, and 0.8] thin films are investigated in this paper. Based on the nonlinear transmittance and femtosecond-transient absorption spectrum measurements, it is found that the $MA_{1-x}FA_xPbI_3$ materials exhibit NLO behavior dependent on excitation intensity. The TPA coefficient of $MA_{1-x}FA_xPbI_3$ decreases with the increase of formamidinium (FA) content, while the relevant saturable intensity increases. In addition, it is revealed that the linear absorption process from valence band 2 to valance band 1 still exists even under a very low excitation intensity. With the increase of excitation intensity, the light transmittance at 1300 nm decreases first and then increases sharply, which also supports the explanation for the coexistence of TPA and SA. It is expected that our findings will promote the application of perovskite materials in nonlinear optoelectronic devices.

https://doi.org/10.1364/PRJ.398975

1. INTRODUCTION

Organic-inorganic halide perovskite materials have attracted great interest due to outstanding optoelectronic properties, such as high carrier mobility [1], as well as tunable photoluminescence (PL) properties [2]. At present, perovskite materials have already achieved great success in the field of photovoltaics. For example, the efficiency of perovskite solar cells can be up to 25.2% [3], which is comparable to that of polycrystalline silicon solar cells [4]. Meanwhile, perovskite materials have been widely used for light-emitting diodes [5,6]. Recently, the excellent nonlinear optical (NLO) properties of organic-inorganic halide perovskite materials have increasingly attracted attention [7]. It is well known that the original molecular polarization of materials resulting from charge transfer between the molecular portion A and BX_3 in perovskite exhibits the electron cloud distortion under intensive light, which leads to NLO properties [8]. Compared with all-inorganic perovskite materials, the organic-inorganic hybrid perovskite with a softer framework allows for the change of A-cation orientation, which may enhance the optical nonlinearity. For instance, a comparative study on the NLO properties of colloidal $MAPbBr_3$(MA = CH_3NH_3) and $CsPbBr_3$ quantum dots (QDs) was conducted by Lu *et al.*, proving that the nonlinear absorption characteristics of organic-inorganic hybrid perovskite QDs are much more pronounced than those of all-inorganic perovskite QDs because of the photoinduced orientation effects [9]. Suárez *et al.* studied the NLO properties of $MAPbX_3$ polycrystalline thin films [10]. It was found that both the nonlinear absorption coefficient (β) and the nonlinear refraction index (n) of organic-inorganic halide perovskite thin films are three to four orders of magnitude larger than that of all-inorganic perovskite $CsPbX_3$, which shows more potential in the field of

NLO application. Additionally, it has been proved that the perovskite $MAPbX_3$ (X = Cl, Br, I) thin film possesses a strong nonlinear absorption coefficient, comparable with the highest reported [11]. Kalanoor *et al.* investigated the NLO properties of the $MAPbI_3$ thin film, which were dominated by bound carriers at lower pump intensities, but they were dominated by free carriers and two-photon absorption (TPA) at higher pump intensities [12].

Although a great progress has been made in the research of the NLO properties of organic-inorganic halide perovskite materials, there are still many unanswered questions. For example, the influences of constituents on the NLO properties in organic-inorganic halide perovskite materials still need further investigation. More importantly, the physical mechanism of coexistence of multiple NLO behaviors in such materials has not yet been well addressed.

In this work, comparative studies on the NLO properties of perovskite [$MA_{1-x}FA_xPbI_3$, FA = $CH(NH_2)_2$, $x = 0$, 0.2, 0.4, 0.6, and 0.8] were carried out by doping the A-site cations of organic-inorganic hybrid perovskite. The conversion process from TPA to saturable absorption (SA) in the $MA_{1-x}FA_xPbI_3$ thin films has been observed at different excitation intensities, whose physical mechanism is then revealed through the measurements of nonlinear transmittance and femtosecond-transient absorption (fs-TA) spectrum.

2. EXPERIMENTAL SECTION

A. Material Preparation

High-purity (99.99%) PbI_2 was purchased from Alfa Chemical Group. Methylammonium iodide (MAI) and formamidinium iodide (FAI) with a purity greater than 99.5% were purchased from Luminescence Technology Corp. To prepare $MA_{1-x}FA_xPbI_3$ ($x = 0$, 0.2, 0.4, 0.6, and 0.8) solutions with a concentration of 1 mol/L, MAI and FAI powders with the corresponding molar ratios, together with PbI_2, were added to dimethylformamide (DMF) and dimethylsulfoxide (DMSO), which had a volume ratio of 7:3. The solutions were stirred at the rate of 300 r/min and heated at 60°C for 2 h. Prior to spin coating on quartz substrates, the solution was filtered with 0.22 μm polytetrafluoroethylene filters. Finally, thin films of about ~100 nm, evaluated by scanning electron microscopy (SEM) via the intramolecular exchange method, were prepared. To avoid the sample degradation, another quartz substrate was used to capsulate the thin film. Pure $FAPbI_3$ has not been synthesized successfully using this method because black α-$FAPbI_3$ is not stable and easily collapses into yellow β-$FAPbI_3$ structures at room temperature. However, the stable structure can be obtained when the proportion of FA is greater than 20%. Thin films fabricated by the above-mentioned method are dense and uniform.

B. Material Characterization

SEM (ZEISS GeminiSEM 300) was used to characterize the morphological properties of $MA_{1-x}FA_xPbI_3$ thin films. X-ray diffraction (XRD) measurements were recorded on a Bruker D8 Discover X-ray diffraction system. The linear absorption spectra were recorded on an ultraviolet–visible–near-infrared spectrophotometer (Lambda 950, PerkinElmer, Inc.) at room temperature.

C. Nonlinear Optical and Ultrafast Dynamics Characterization

During the open-aperture (OA) Z-scan measurements, femtosecond pulses (100 fs, 1000 Hz) at 800 nm were focused on the samples by a spherical lens with a 500 mm focal length, and the transmitted light was then measured by a silicon detector. For the measurements of power-dependent transmittance, the fs pulses first passed through an electric ultrafast broadband variable attenuator (Newport VA-BB–4–CONEX) and were then focused onto the samples. The transmitted light was again collected by the silicon detector. The ultrafast dynamics of perovskite materials was investigated using a standard fs-TA spectroscopy excited at 1300 nm pulses (100 fs, 1000 Hz). The excited light spot area was ~0.002 cm^2, while the spot area of probe light was ~0.0005 cm^2.

3. RESULTS AND DISCUSSION

Figure 1(a) presents the XRD patterns of the $MA_{1-x}FA_xPbI_3$ ($x = 0$, 0.2, 0.4, 0.6, and 0.8) thin films on quartz substrates. Structural changes are observed for the peaks at 14.10°, 19.95°, 24.41°, 28.50°, and 31.90°, respectively. Due to the larger size of FA cation, the crystal lattice will expand when MA is replaced by FA cation. Therefore, all peaks will shift slightly to smaller diffraction angles with the increase of FA content. This gradual blue shift of the diffraction angle (rather than the appearance of two separate peaks with variable intensities) is a strong indication that a mixed phase of $MA_{1-x}FA_xPbI_3$ is formed, where the two cations both exist in the same lattice frame. It is worth noting that for $MAPbI_3$, there is a peak at 23.45°, which is one of the characteristics of the tetragonal phase [13]. However, no such peaks for the other four samples can be detected, which suggests the cubic phase of $MAPbI_3$. As shown in Fig. 1(b), the $MA_{1-x}FA_xPbI_3$ thin films exhibit two absorption bands at ~480 and ~775 nm, which implies that they possess a three-level band structure composed by a dual valence band (VB) and a single conduction band (CB) [14]. Furthermore, a continuous shift of the absorption bands to a longer wavelength with the increase of FA content is observed, which further proves the successful fabrication of mixed organic cation perovskites. The inset of Fig. 1(b) shows the SEM image of $MA_{0.2}FA_{0.8}PbI_3$, and it can be clearly seen that the thickness of the thin film is about 100 nm.

It is noted that there are no NLO signals recorded for the quartz substrates under different excitation powers, which ensures the observed NLO behavior mainly originates from the

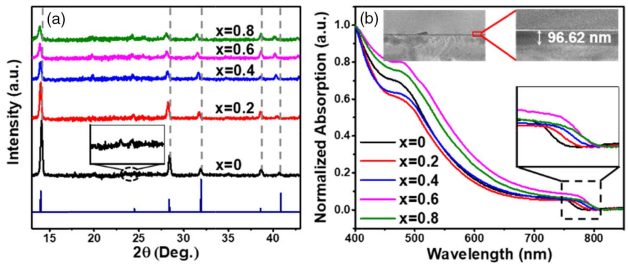

Fig. 1. (a) XRD patterns and (b) normalized ultraviolet–visible absorption spectra of organic–inorganic perovskite $MA_{1-x}FA_xPbI_3$ ($x = 0$, 0.2, 0.4, 0.6, and 0.8); inset is the SEM image of $MA_{0.2}FA_{0.8}PbI_3$.

perovskite materials. Typical OA Z-scan measurements for $MA_{1-x}FA_xPbI_3$ ($x = 0$, 0.2, 0.4, 0.6, and 0.8) at an excitation intensity of 0.8 GW/cm^2 were carried out, in which strong nonlinear absorption was observed for all the samples [Fig. 2(a)]. To be specific, a valley–hump–valley structured curve was only observed in the $MAPbI_3$ thin film, while the other four samples exhibited simple-valley-structured curves. However, under the excitation of a higher power intensity ($I_0 = 1.2$ GW/cm^2), the samples exhibit valley–hump–valley structured curves, indicating the coexistence of multiple nonlinear absorption effects. With a further increase in excitation intensity, the SA will dominate in the NLO process. To clearly express the NLO conversion process, as an example, the relevant power-dependent Z-scan data for the $MA_{0.2}FA_{0.8}PbI_3$ thin film are presented in Fig. 2(b). The similar phenomenon has been reported in previous literature [15–17]. It is well known that the reverse saturable absorption (RSA) behavior is mainly contributed by TPA. Therefore, the TPA mechanism may also hold true for the nonlinear behavior of our $MA_{1-x}FA_xPbI_3$ thin films at low excitation intensity.

The conversion mechanism from TPA to SA can be revealed by using fs-TA spectroscopy. Considering that the absorption band edges of the samples are at around 775 nm, the excitation wavelength at 1300 nm was selected, to exclude the influences of direct transition from the valance band to conduction band. By tracking the corresponding bleaching recovery process, the photogenerated carrier dynamics in $MA_{1-x}FA_xPbI_3$ thin films can be investigated. Taking the $MA_{0.2}FA_{0.8}PbI_3$ thin film as an example, the fs-TA spectrum in Fig. 3(a) shows the recovery

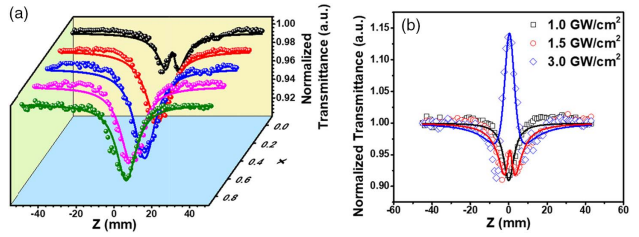

Fig. 2. (a) OA Z-scan results for $MA_{1-x}FA_xPbI_3$ ($x = 0$, 0.2, 0.4, 0.6, and 0.8) at 1.0 GW/cm^2; (b) OA Z-scan results for $MA_{0.2}FA_{0.8}PbI_3$ at $I_0 = 1.0$ GW/cm^2 (squares); 1.5 GW/cm^2 (circles); and 3.0 GW/cm^2 (diamonds).

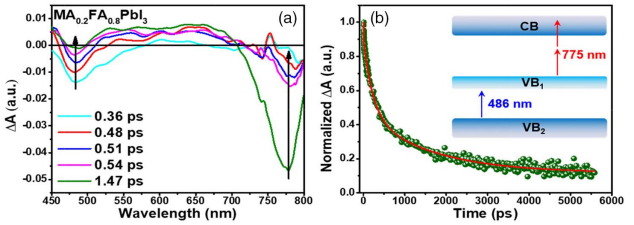

Fig. 3. (a) fs-TA spectra of $MA_{0.2}FA_{0.8}PbI_3$ at different probe-delayed times following the 1300 nm laser excitation with an energy density of 2.0 GW/cm^2. (b) Kinetic profiles of 775 nm bleaching recovery. Inset is a schematic of proposed band structure of $MA_{0.2}FA_{0.8}PbI_3$, showing the dual VBs that give rise to the photoinduced bleaching at 486 and 775 nm.

dynamics of its photoinduced bleaching, in which the two bleaching bands at 486 and 775 nm correspond to the absorption bands in Fig. 1(b), respectively, which proves the existence of dual VBs in $MA_{1-x}FA_xPbI_3$. The bleaching band at 486 nm appears in a short time of ~0.36 ps, and its intensity gradually decreases as time increases. However, the bleaching band at 775 nm does not show any signal until 0.51 ps, and its intensity subsequently increases with the increase of time. This implies that the photoinduced carriers in $MA_{0.2}FA_{0.8}PbI_3$ have undergone two different transition processes. When the laser pulses arrive, electrons in the two valence bands will be excited simultaneously, which will induce the first transition from VB_1 to VB_2. In principle, the two bleaching peaks (486 and 775 nm) should appear at the same time. However, it is noted that the transition time of electrons from VB_1 to VB_2 is around 0.3 ps [18], and the time for VB_1 to fully bleach is 0.36 ps [as shown in Fig. 3(a)]. Therefore, at this moment, the vacancies in VB_2 are occupied by the excited electrons from VB_1. For this reason, no bleaching signal appears. After VB_1 is completely bleached, that is, after 0.36 ps, the bleaching signal of VB_2 will appear. The normalized kinetic profile of the band-edge transitions at 775 nm is shown in Fig. 3(b). As shown in the schematic diagram of the band structure illustrated in the inset of Fig. 3(b), considering the band gap between VB_1 and VB_2 [13], the electrons transition rules and the nonlinear absorption signals in Z-scan measurements, at the excitation wavelength of 1300 nm (0.95 eV), electrons in VB_2 (486 nm) first are excited to VB_1 (775 nm) through single-photon absorption, which are then excited to CB through the TPA process. This explanation is consistent with the nonlinear behavior observed in the Z-scan measurement. Under low power excitation at 800 nm (1.55 eV), the TPA in Z-scan measurement should be due to the transition from VB_1 to CB (1.6 eV). With the increase of excitation intensity, the electron population in the CB gradually becomes saturated, and the excessive photons that cannot be absorbed will pass through thin films directly, resulting in the occurrence of SA. It should be noted that there is no nonlinear signal in the Z-scan measurement excited at a very low intensity ($0 < I_0 < 0.5$ GW/cm^2), which is consistent with the fact that the TPA occurs at a relatively higher excitation intensity.

The conversion of nonlinear absorption processes can be explained by defining a nonlinear absorption coefficient $\alpha(I)$, which is a sum of independent positive (due to SA) and negative (due to RSA) transmission coefficients. The total absorption coefficient for the perovskite materials can be described by [19]

$$\alpha(I) = \frac{\alpha_0}{1 + I/I_{\text{sat}}} + \beta I, \tag{1}$$

where α_0 denotes the linear absorption coefficient, I represents the total input intensity, I_{sat} stands for the saturation intensity, and β is the TPA coefficient. As for the OA Z-scan measurement, the normalized transmittance can be expressed as [20]

$$T(z) = \sum_{m=0}^{\infty} \frac{\left(\frac{-\alpha I_0 L_{\text{eff}}}{1+z^2/z_0^2}\right)^m}{m+1}, \tag{2}$$

where $L_{\text{eff}} = (1 - e^{-\alpha_0 L})/\alpha_0$, z is the longitudinal displacement of the sample from the focus ($z = 0$), I_0 is the on-axis peak

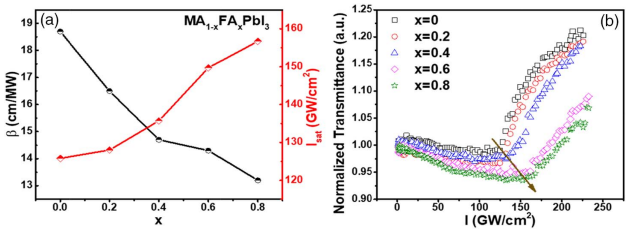

Fig. 4. (a) Doping concentration x-dependent nonlinear absorption coefficient β and saturation intensity I_{sat} for $MA_{1-x}FA_xPbI_3$ ($x = 0$, 0.2, 0.4, 0.6, and 0.8); (b) excitation-intensity-dependent normalized transmittance for $MA_{1-x}FA_xPbI_3$ ($x = 0$, 0.2, 0.4, 0.6, and 0.8).

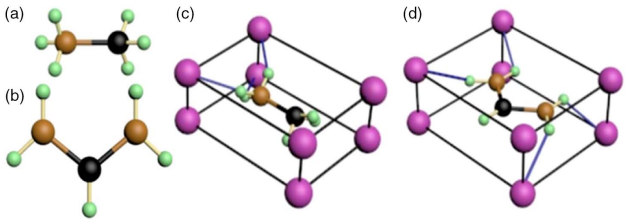

Fig. 5. (a), (b) Structure of MA (methylammonium) and FA (formamidinium) cations. Unit cell structure of (c) $MAPbI_3$ and (d) $FAPbI_3$. Iodine (purple) at cell corners, carbon (black), nitrogen (brown), and hydrogen (light green). NH–I hydrogen bonds are shown as blue lines.

intensity at the focus, L_{eff} is the effective interaction length, L is the sample length, and z_0 is the Rayleigh diffraction length. Theoretical fit of the experimental data could be conducted by the substitution of Eq. (1) into Eq. (2).

The fitting results of the nonlinear absorption coefficient β and saturation intensity I_{sat} for $MA_{1-x}FA_xPbI_3$ are displayed in Fig. 4(a). Both β and I_{sat} show a strong dependence on the doping concentration (x) of FA. As the value of x increases from 0 to 0.8, β reduces from 18.7 to 13.2 cm/MW, while I_{sat} increases from 125.8 to 156.7 GW/cm^2. Figure 4(b) shows the excitation-intensity-dependent normalized transmittance for $MA_{1-x}FA_xPbI_3$ at 1300 nm, which first decreases slightly and then increases sharply, as a result of the TPA saturation followed by the SA process. In addition, even under very low excitation power, the normalized transmittance of $MA_{1-x}FA_xPbI_3$ still decreases, indicating the presence of absorption. Considering the intensity range of excitation-intensity transmittance includes that of Z-scan, and there is no signal in the Z-scan curve under the same intensity, it could be concluded that the absorption-induced transmittance decrease at low excitation intensity in the $MA_{1-x}FA_xPbI_3$ thin films should be caused by the single-photon transition from VB_2 to VB_1, instead of TPA from VB to CB.

Previous literature mainly focused on the effects of A-site cations in $MA_{1-x}FA_xPbI_3$ ($0 \le x \le 1$) on their NLO properties. In addition, previous results have demonstrated the influence of the expansion in the unit cell [21] and the increase in the number of hydrogen bonding [22,23] on the properties of $MA_{1-x}FA_xPbI_3$, which is caused by the introduction of FA cation. The structures of MA, FA, $MAPbI_3$, and $FAPbI_3$ are given in Fig. 5. When FA is coordinated with $[PbI_6]^{4-}$ octahedron to form a perovskite structure, due to its larger size, the unit cell will expand, resulting in a more significant octahedral distortion. This degree of distortion will change with different ratios of MA and FA, which directly leads to the increase of the Pb–I bond length and the Pb–I–Pb bond angle [21], weakening the traction of I^- to Pb^{2+} and reducing Pb^{2+} electron cloud distortion. Apart from this, hydrogen bonds also play an important role in material properties. It has been found that hydrogen atoms allow the iodides to move closer together so that they can bridge two iodide sites in organic-inorganic hybrid perovskite [24] (analogous behavior has been discussed in oxide perovskites [25]), reducing the interaction between I^- and Pb^{2+}. Although the hydrogen bonds formed by MA may be slightly stronger than by FA, the number of hydrogen bonds (NH–I) is determined by the hydrogen atoms carried by N atoms. Therefore, FA cations have a higher propensity to form hydrogen bonds [22,23]. The formation of more hydrogen bonds caused by the incorporation of FA will further weaken the Pb–I bond, leading to the weaker distortion of the Pb^{2+} electron cloud. It is well known that the NLO properties originate from the electron cloud distortion. In addition, it has been confirmed that the NLO properties of $MA_{1-x}FA_xPbI_3$ ($x = 0$, 0.2, 0.4, 0.6, and 0.8) materials were determined by their CBs,

Table 1. Calculated Nonlinear Optical Parameters of $MA_{1-x}FA_xPbI_3$ and Other Materials Reported Elsewhere

Material	Excitation Wavelength (nm)	β (cm/MW)	I_{sat} (GW/cm^2)	Ref.
$CsPbBr_3$ (QDs)	800 (fs)	-1.71×10^{-3}	–	[7]
$MAPbBr_3$ (QDs)		4.18×10^{-3}	–	
$MAPbX_3$	532 (ns)	0.5	800	[11]
$MAPbI_3$	514 (fs)	18.5	–	[12]
	1028 (fs)	110	–	
Au (NP array)	800 (fs)	0.588	210	[15]
Alkoxy phthalocyanines		1.5	–	[16]
GaAs	1680 (fs)	2.5×10^{-3}	–	[26]
Pt (NPs)	532 (ns)	3.2×10^{-2}	1.1×10^{-3}	[27]
$CsPbBr_3$ (NCs)	800 (fs)	9.7×10^{-5}	–	[28]
$MAPbI_3$ (SC)		8.6×10^{-3}	–	[29]
$MAPbI_3$	1064 (fs)	−2.03	12.61	[30]
$C_6H_5CH_2NH_3PbBr_3$ (microdisks)	800 (fs)	1.4×10^{-6}	84.3	[31]
$FAPbBr_3$ (NCs)	800 (fs)	4.2×10^{-6}	–	[32]
$MA_{1-x}FA_xPbI_3$	800 (fs)	18.7–13.2	125.8–157.1	This work

which are contributed by the p orbit of Pb^{2+} [33]. As a result, the reduced distortion of the electron cloud of Pb^{2+} leads to the decrease of the nonlinear absorption coefficient.

For comparisons, the nonlinear absorption coefficient β and saturated absorption intensity I_{sat} of different materials are summarized in Table 1, including the perovskite single crystal, nanocrystals, III–V semiconductor, metal nanoparticle, etc. Among all of them, the nonlinear absorption coefficients β of $MA_{1-x}FA_xPbI_3$ ($x = 0$, 0.2, 0.4, 0.6, and 0.8) are overall several orders of magnitude larger than those of other materials. It is worth noting that the nonlinear absorption coefficient is closely related to the crystal structure and quality, sample thickness [34], and nonradiative energy transfer [7]. The larger nonlinear absorption coefficient of our perovskite thin films implies the huge development prospects in nonlinear optical applications.

4. CONCLUSION

In summary, the NLO properties of perovskite $MA_{1-x}FA_xPbI_3$ ($x = 0$, 0.2, 0.4, 0.6, and 0.8) have been investigated. They exhibit strong doping concentration-dependent NLO properties, and a giant nonlinear absorption coefficient up to 18.7 cm/MW was achieved with a doping concentration of $x = 0$. With the x increase, as a result of the cell volume expansion and the formation of more hydrogen bonds, the TPA coefficient of $MA_{1-x}FA_xPbI_3$ gradually decreases, while the saturation intensity gradually increases. Our study provides a strategy to enhance the NLO properties of organic-inorganic hybrid perovskites via doping A-cation, which is vital for the application in the field of nonlinear optical devices.

Funding. National Natural Science Foundation of China (61605073, 61935017, 91733302); Universidade de Macau (MYRG2018-00148-IAPME); The Science and Technology Development Fund (091/2017/A2); Science, Technology and Innovation Commission of Shenzhen Municipality (JCYJ20180305180553701, JCYJ20190808121211510, KQTD2015071710313656).

Disclosures. The authors declare no conflicts of interest.

REFERENCES

1. G. Xing, N. Mathews, S. Sun, S. S. Lim, Y. M. Lam, M. Grätzel, S. Mhaisalkar, and T. C. Sum, "Long-range balanced electron-and hole-transport lengths in organic-inorganic $CH_3NH_3PbI_3$," Science **342**, 344–347 (2013).
2. Z. Chen, C. Zhang, X. F. Jiang, M. Liu, R. Xia, T. Shi, D. Chen, Q. Xue, Y. J. Zhao, and S. Su, "High-performance color-tunable perovskite light emitting devices through structural modulation from bulk to layered film," Adv. Mater. **29**, 1603157 (2017).
3. S. Florent, W. Jérémie, B. A. Kamino, M. Bräuninger, R. Monnard, B. Paviet-Salomon, L. Barraud, L. Ding, J. J. D. Leon, D. Sacchetto, G. Cattaneo, M. Despeisse, M. Boccard, S. Nicolay, Q. Jeangros, B. Niesen, and C. Ballif, "Fully textured monolithic perovskite/silicon tandem solar cells with 25.2% power conversion efficiency," Nat. Mater. **17**, 820–826 (2018).
4. M. A. Green, "The path to 25% silicon solar cell efficiency: history of silicon cell evolution," Prog. Photovolt. Res. Appl. **17**, 183–189 (2010).
5. Y. Kim, H. Cho, J. H. Heo, T. Kim, N. Myoung, C. Lee, S. H. Im, and T. Lee, "Multicolored organic/inorganic hybrid perovskite light-emitting diodes," Adv. Mater. **27**, 1248–1254 (2015).
6. A. Perulli, A. Balena, M. Fernandez, G. Nedelcu, M. V. Kovalenko, M. Lomascolo, and M. Anni, "Full color tuning in binary polymer: perovskite nanocrystals organic-inorganic hybrid blends," Appl. Phys. Lett. **112**, 171904 (2018).
7. J. Wang, Y. Mi, X. Gao, J. Li, J. Li, S. Lan, C. Fang, H. Shen, X. Wen, R. Chen, X. Liu, T. He, and D. Li, "Giant nonlinear optical response in 2D perovskite heterostructures," Adv. Opt. Mater. **7**, 1900398 (2019).
8. K. Wei, T. Jiang, Z. J. Xu, J. H. Zhou, J. You, Y. X. Tang, H. Li, R. Z. Chen, X. Zheng, S. S. Wang, K. Yin, Z. Y. Wang, J. Wang, and X. Cheng, "Ultrafast carrier transfer promoted by interlayer coulomb coupling in 2D/3D perovskite heterostructures," Laser Photon. Rev. **12**, 1800128 (2018).
9. W. Lu, C. Chen, D. Han, L. Yao, J. Han, H. Zhong, and Y. Wang, "Nonlinear optical properties of colloidal $CH_3NH_3PbBr_3$ and $CsPbBr_3$ quantum dots: a comparison study using Z-scan technique," Adv. Opt. Mater. **4**, 1732–1737 (2016).
10. I. Suarez, M. Vallespelarda, A. F. Gualdronreyes, I. Morasero, A. Ferrando, H. Michinel, J. R. Salgueiro, and J. P. M. Pastor, "Outstanding nonlinear optical properties of methylammonium-and Cs-PbX_3 (X = Br, I, and Br-I) perovskites: polycrystalline thin films and nanoparticles," APL Mater. **7**, 041106 (2019).
11. R. A. Ganeev, K. S. Rao, Z. Yu, W. Yu, C. Yao, Y. Fu, K. Zhang, and C. Guo, "Strong nonlinear absorption in perovskite films," Opt. Mater. Express **8**, 1472–1483 (2018).
12. B. S. Kalanoor, L. Gouda, R. Gottesman, S. Tirosh, E. Haltzi, A. Zaban, and Y. R. Tischler, "Third-order optical nonlinearities in organometallic methylammonium lead iodide perovskite thin films," ACS Photon. **3**, 361–370 (2016).
13. B. Slimi, M. Mollar, I. B. Assaker, I. Kriaa, R. Chtourou, and B. Marí, "Perovskite $FA_{1-x}MA_xPbI_3$ for solar cells: films formation and properties," Energy Proc. **102**, 87–95 (2016).
14. J. S. Manser and P. V. Kamat, "Band filling with free charge carriers in organometal halide perovskites," Nat. Photonics **8**, 737–743 (2014).
15. K. Wang, H. Long, M. Fu, G. Yang, and P. Lu, "Intensity-dependent reversal of nonlinearity sign in a gold nanoparticle array," Opt. Lett. **35**, 1560–1562 (2010).
16. N. Venkatram, D. N. Rao, L. Giribabu, and S. V. Rao, "Femtosecond nonlinear optical properties of alkoxy phthalocyanines at 800 nm studied using Z-scan technique," Chem. Phys. Lett. **464**, 211–215 (2008).
17. Q. Ouyang, H. Yu, K. Zhang, and Y. Chen, "Saturable absorption and the changeover from saturable absorption to reverse saturable absorption of MoS_2 nanoflake array films," J. Mater. Chem. C **2**, 6319–6325 (2014).
18. P. Piatkowski, B. Cohen, S. Kazim, S. Ahmad, and A. Douhal, "How photon pump fluence changes the charge carrier relaxation mechanism in an organic-inorganic hybrid lead triiodide perovskite," Phys. Chem. Chem. Phys. **18**, 27090 (2016).
19. J. Wang, Y. Hernandez, M. Lotya, J. N. Coleman, and W. J. Blau, "Broadband nonlinear optical response of graphene dispersions," Adv. Mater. **21**, 2430–2435 (2009).
20. M. Sheik-Bahae, A. A. Said, T. H. Wei, D. J. Hagan, and V. E. W. Stryland, "Sensitive measurement of optical nonlinearities using a single beam," IEEE J. Quantum Electron. **26**, 760–769 (1990).
21. F. Bi, X. Zheng, and C. Yam, "First-principles study of mixed cation methylammonium-hybrid perovskite," Acta Phys. Chim. Sin. **35**, 69–75 (2019).
22. A. Amat, E. Mosconi, E. Ronca, C. Quarti, P. Umari, M. K. Nazeeruddin, M. Grätzel, and F. Angelis, "Cation-induced band-gap tuning in organohalide perovskites: interplay of spin-orbit coupling and octahedra tilting," Nano Lett. **14**, 3608–3616 (2014).
23. M. T. Weller, O. J. Weber, J. M. Frost, and A. Walsh, "Cubic perovskite structure of black formamidinium lead iodide, α-$[HC(NH_2)_2]PbI_3$, at 298 K," J. Phys. Chem. Lett. **6**, 3209–3212 (2015).

24. D. A. Egger, L. Kronik, and A. M. Rappe, "Theory of hydrogen migration in organic-inorganic halide perovskites," Angew. Chem. **127**, 12614–12618 (2015).
25. M. S. Islam, R. A. Davies, and J. D. Gale, "Proton migration and defect interactions in the $CaZrO_3$ orthorhombic perovskite: a quantum mechanical study," Chem. Mater. **13**, 2049–2055 (2001).
26. W. C. Hurlbut and Y.-S. Lee, "Multiphoton absorption and nonlinear refraction of GaAs in the mid-infrared," Opt. Lett. **32**, 668–670 (2007).
27. Y. Gao, X. Zhang, Y. Li, H. Liu, Y. Wang, Q. Chang, W. Jiao, and Y. Song, "Saturable absorption and reverse saturable absorption in platinum nanoparticles," Opt. Commun. **251**, 429–433 (2005).
28. Y. Wang, X. Li, X. Zhao, L. Xiao, H. Zeng, and H. Sun, "Nonlinear absorption and low-threshold multiphoton pumped stimulated emission from all-inorganic perovskite nanocrystals," Nano Lett. **16**, 448–453 (2015).
29. F. O. Saouma, D. Y. Park, S. H. Kim, M. S. Jeong, and J. I. Jang, "Multiphoton absorption coefficients of organic-inorganic lead halide perovskites $CH_3NH_3PbX_3$ (X = Cl, Br, I) single crystals," Chem. Mater. **29**, 6876–6882 (2017).
30. R. Zhang, J. Fan, X. Zhang, H. Yu, H. Zhang, Y. Mai, T. Xu, J. Wang, and H. J. Snaith, "Nonlinear optical response of organic-inorganic halide perovskites," ACS Photon. **3**, 371–377 (2016).
31. A. Mushtaq, D. Kushavah, S. Ghosh, and S. K. Pal, "Nonlinear optical properties of benzylamine lead (II) bromide perovskite microdisks in femtosecond regime," Appl. Phys. Lett. **114**, 051902 (2019).
32. L. Yang, K. Wei, Z. J. Xu, F. M. Li, R. Z. Chen, X. Zheng, X. Cheng, and T. Jiang, "Nonlinear absorption and temperature-dependent fluorescence of perovskite $FAPbBr_3$ nanocrystal," Opt. Lett. **43**, 122–125 (2018).
33. Y. Q. Liu, H. L. Cui, and D. S. Wei, "Effects of spin-orbit coupling on nonequilibrium quantum transport properties of hybrid halide perovskites," J. Phys. Chem. C **122**, 4150–4155 (2018).
34. R. Wang and J. Wei, "Dependence of the readout resolving on the thickness of nonlinear super-resolution thin films," Proc. SPIE **8782**, 878205 (2013).